Microstructure and Mechanical Properties of Asymmetrically Rolled High-Purity Titanium Ultra-Thin Strips

Fengmei Bai[a,b], Jiale Wang[a,b], Yan Wu[a,b], Junxian Gu[d], Zhihan Lu[a,b], Fengju Zhang[a,b],

Hongwei Zhou[c] ⓘ *, Jingqi Chen[e], Hongbo Pan[a*]* ⓘ

[a]Anhui University of Technology, Anhui Province Key Laboratory of Metallurgical Engineering & Resources Recycling, 243002, Maanshan, China.
[b]Anhui University of Technology, School of Metallurgical Engineering, 243002 Maanshan, China.
[c]Anhui University of Technology, School of Materials Science and Technology, 243002 Maanshan, China.
[d]Hangzhou Turbine Power Group Co., Quality Assurance Department, Hangzhou, China.
[e]Yanshan University, National Engineering Research Center for Equipment and Technology of Cold Rolled Strip, 066004, Qinhuangdao, China.

In this work, the asymmetrical rolling of 860 μm thick high-purity titanium (HP-Ti) strips is investigated. HP-Ti ultra-thin strips are produced in thicknesses ranging from 280 μm to 20 μm. The microstructure and texture evolution of HP-Ti ultra-thin strips were analyzed using electron backscattering diffraction (EBSD), transmission electron microscopy (TEM), and X-ray diffraction (XRD). The raw strips have a homogeneous and equiaxed microstructure, containing some face-centered cubic (FCC) Ti laths. With a rise in rolling reduction, equiaxed grains change into deformation structures characterized by a high density of dislocations. The formation of an ultra-fine grained microstructure and the elimination of FCC-Ti laths come next. The influence of grain rotation and slip systems on the development of texture in ultra-thin strips during rolling reduction is illustrated through the analysis of {0002} pole figures and orientation distribution function. The tensile qualities of ultra-thin strips are correlated with their microstructure.

Keywords: *High-purity titanium, ultra-thin strip, asymmetric rolling, microstructure, mechanical property.*

1. Introduction

The rapid growth of Micro Electro-Mechanical System (MEMS) technology in recent years has resulted in the miniaturization of raw materials and parts for electronic devices, bio-robots, micro-air vehicles, various sensors, and so on. The demand for micromaterials such as ultra-thin strips and their fabrication procedures is increasing[1-3]. There are several methods for producing ultra-thin strips, including rolling and electrolysis. The rolling approach offers numerous benefits, including energy savings and environmental conservation. At the moment, multi-roller mills such as the Senjimir mill are used to roll ultra-thin strips, which has a high price and a complex rolling process, and the preparation cost of ultra-thin strips is high. Liu et al.[2,4-8] independently created a micro-forming mill and successfully rolled a variety of ultra-thin strips such as copper, aluminum, stainless steel, and titanium. During this procedure, both metals and alloys exhibit great extensibility[7].

Commercially pure titanium (CP-Ti) undergoes significant grain refinement during severe plastic deformation (SPD) at room temperature, such as equal channel angular extrusion (ECAE), multipass rolling, and accumulative roll-bonding (ARB) process. Zherebtsov et al.[9] investigated the evolution of the microstructure in CP-Ti during plane-strain multipass rolling. The microstructure of CP-Ti is homogeneous and equiaxed, with an average grain size of 15 μm. Deformation was accompanied by twinning during multipass rolling to a low strain. Rolling to a true strain of 2.66 produced a microstructure with a grain/subgrain size of ~200 nm. Terada et al.[10] found that the microstructure of the CP-Ti specimens showed two types of characteristic ultrafine microstructures when CP-Ti with the mean grain size of 10 μm was deformed by accumulative roll-bonding (ARB) process. The first was the lamellar boundary structure elongated along RD, and the second was equiaxed grains with mean grain size of 80–100 nm. The fraction of equiaxed grains increased as the ARB process proceeded, and after 8 ARB cycles (equivalent strain of 6.4) 90% of the specimen was filled with the equiaxed grains. The tensile strength increased while the total elongation decreased as the number of ARB processes increased. Wang et al.[11] carried out ECAP experiments on CP-Ti with an average grain size of 26 μm. After the second ECAP pass, the dislocation density and subgrain quantity are significantly higher than after first pass. The dislocation density decreases after the third pass, the number of subgrain increases. After four passes, the grains are refined to 170 nm. At low strains, twinning is

the dominant deformation mechanism during large plastic deformation at room temperature, whereas dislocations are the dominant deformation mechanism and promote grain refinement at high strains.

Many studies have found that when CP-Ti is subjected to SPD such as cold-rolling and tensile testing[8,12-14], the hexagonal close-packed (HCP) transforms to face-centered cubic (FCC). The semi-coherent orientation relationship (OR) between the HCP and FCC phases meets $\left\{10\overline{1}0\right\}_\alpha //\left\{2\overline{2}0\right\}_{FCC}$ and $1\overline{2}10_\alpha //110_{FCC}$ [8,12,13]. As is well known, HCP-α and BCC-β (body-centered cubic) phases in titanium alloys obey Burgers OR, i.e., $\left\{0001\right\}_\alpha //\left\{110\right\}_\beta$ and $11\overline{2}0_\alpha //111_\beta$ [15]. The α/β interphase boundaries are semi-coherent OR[16]. Bai et al.[12] observed that the FCC/HCP phase interface slides and rotates under cold-rolling, causing a deviation from the semi-coherent OR. FCC phase is dynamically recrystallized as strain increases, and bands are transformed into equiaxed grains. Simultaneously, reverse transformation of FCC to HCP appears, resulting in a reduction of FCC phase.

CP-Ti has an axial ratio c/a of 1.587, which is less than the ideal axial ratio of 1.633, and this type of hexagonal structure metal will form a TD-split type basal texture with a characteristic tilt of ±20°-±40° from the ND to the TD during deformation[17-19]. Chun et al.[17] investigated the evolution of texture during cold rolling of CP-Ti with a focus on deformation twinning and dislocation slip. Slip and twinning accommodated external strain for low to intermediate deformation up to 40% in thickness reduction. Twinning in this stage weakens the texture component by randomizing crystal orientations. Slip overrode twinning and the texture of deformed specimens was strengthened by slip, resulting in a split-basal texture with a ±35° tilt from the ND to the TD direction in heavily deformed specimens. Gurao et al.[20] noticed that the CP-Ti will have different textures depending on strain path when cold-rolled. When unidirectional rolling and reverse rolling are performed, a split-bimodal basal texture with a characteristic tilt of ±35° from the ND to the TD direction. The cross-rolled samples, on the other hand, have a more typical basal texture.

We used asymmetrical rolling to manufacture the thinnest 10 μm HP-Ti ultra-thin strip[8,12]. However, the mechanisms of microstructure and texture evolution during asymmetrical rolling remains unknown. Wang et al.[14] investigated the room-temperature tensile properties of recrystallized commercially pure (CP) Ti strips with thicknesses ranging from 200 μm to

5 μm. The mechanical properties of HP-Ti ultra-thin strips in the cold-rolled state have received little attention. In this paper, asymmetrical rolling at room temperature was used to create a series of ultra-thin HP-Ti strips with thicknesses ranging from 280 μm to 20 μm. The tensile properties of ultra-thin strips, as well as the evolution of dislocation structure and texture, were examined.

2. Experimental Methods and Procedure

High purity Ti (HP-Ti) sheets of 11 mm × 30 mm × 60 mm size were cold-rolled into thin strips with a thickness of 860 μm with about 92% total reduction in thickness. The recrystallized thin strips were obtained after annealing at 500 °C for 1 h under Argon protection[12]. Through the use of an asymmetrical rolling mill[7], the HP-Ti thin strip was cold-rolled with asymmetry ratio of 1.2 to create a series of ultra-thin strip specimens with thicknesses ranging from 280 μm to 20 μm[8,12], and the corresponding accumulated strain is 67.4%, 89.0%, 92.4%, 96.5%, and 97.8%, respectively.

The rolled surface of the material as received was examined using a HKL Symmetry EBSD on a Zeiss Sigma 500 scanning transmission electron microscope. A Talos FEI F200x TEM was used to observe the microstructure of the ultra-thin HP-Ti strips. By using a fully automatic X-ray diffractometer, the X'Pert Pro, macro-textures of ultra-thin strips were examined. INSTRON 5969 universal testing equipment were used to evaluate the tensile characteristics of ultra-thin strips. Figure 1 depicts the tensile testing specimens' dimensions.

The mechanical grinding, mechanical polishing, and final electropolishing of the EBSD samples took place at room temperature for 1-2 minutes while using a voltage of 35 V and a solution of 94% glacial acetic acid and 6% perchloric acid. Samples with a diameter of 3 mm and a thickness of 50 μm were processed by ion milling after mechanical polishing was used to make the TEM specimens.

3. Results and Discussion

3.1. Microstructure of the as-received HP-Ti strip

The inverse pole figure (IPF) and the size distribution of the as-received HP-Ti thin strip are shown in Figure 2. The microstructure in the as-received condition consists of equiaxed grains with an average size of 6.2 μm. The
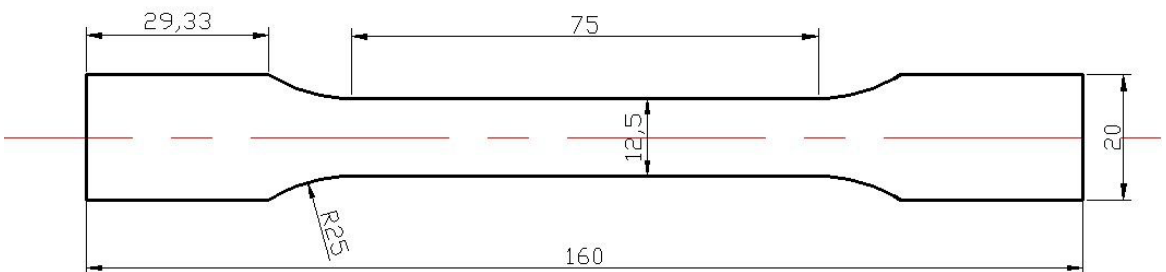

Figure 1. Geometry of tensile test specimen (unit: mm).

microstructure of the raw material is twin-free. Figure 2c displays the pole figures (PFs) of the annealed HP-Ti strip with a basal texture of the TD-split type(the c-axis tilted 30° from ND to TD), which is a common texture in cold-rolled pure Ti[17,18] and recrystallized CP-Ti sheets[19].

Figure 3 displays the TEM images of the raw material. Bright field image (Figure 3a) and dark field image reveal lath-like microstructures within the grains (Figure 3b). These lath-like microstructures are face-centered cubic (FCC) Ti with an orientation relationship to the HCP phase, according to examination of a selected area electron diffraction (SAED) pattern in Figure 3c. The HCP-FCC phase transition is caused by the Shockley partial dislocation sliding along the direction $\frac{1}{6}\langle\overline{1}2\overline{1}0\rangle$ on the prism plane $(10\overline{1}0)_\alpha$ [8,12], which is consistent with the results of molecular dynamics theory calculation[15], first principles calculation and TEM analysis[13,21,22]. For CP-Ti and its alloys, the HCP to FCC phase transformation has been seen during annealing as well as plastic deformation[14,23,24]. HCP Zr alloy[25,26] also exhibited this phase transformation.

The results of transmission Kikuchi diffraction (TKD) of annealed HP-Ti thin strip are shown in Figure 4. The yellow band marked in Figure 4a is FCC phase, and the remaining red areas are HCP phase. Both IPF map (Figure 4b) and Kikuchi band contrast map (Figure 4c) exhibit a distinct FCC phase. As can be seen from Figure 4, the FCC phase presents a banded distribution, which is consistent with the results observed by TEM in Figure 3. The content of FCC phase is about 9.5%. Figures 4d and 4e are the PFs of the FCC phase marked as 1 and the adjacent HCP grains in Figure 4a,

respectively. PFs analysis shows that FCC/HCP phases meet the same orientation relationship as the results in the SAED pattern in Figure 3c: $[0001]_\alpha //[001]_{FCC},(10\overline{1}0)_\alpha //(110)_{FCC}$.

3.2. Microstructure evolution under rolling

The TEM images of the 280 μm ultra-thin strip are shown in Figure 5a–c. A deformed structure with a high dislocation density is formed in comparison to the microstructure of the raw material. Local grains have undergone great refinement. Figure 5b displays cells that are about 1 μm in size. The laths are FCC phase, with a lattice constant of 0.425 nm, according to a SEAD pattern analysis in Figure 5c. The matrix HCP and FCC phase have an orientation relationship of $[0001]_\alpha //[001]_{FCC}$ and $(10\overline{1}0)_\alpha //(110)_{FCC}$, which is similar with the findings reported in the literature[8,12]. The TEM images of the 95 μm ultra-thin strip are shown in Figure 5d–f. The deformed structure in Figure 5d is more uniform than the 280 μm ultra-thin strip. The microstructure also revealed subgrains /grains with blurred boundaries. Additionally, some residual FCC laths can still be seen in Figure 5(e,f), and there are fewer FCC laths overall, which suggests that throughout the asymmetrical rolling process, the FCC laths go through plastic deformation and spheroidization[12].

When the ultra-thin strip is further rolled to a thickness of 65 μm, the microstructure is seen in Figure 6(a, b). Individual subgrains with sizes ranging from 200 to 450 nm are also seen, but their boundaries are unclear. Figure 6b shows a small number of FCC laths; The width and length of these laths are considerably smaller than those of the 280 μm and 95 μm ultra-thin strips.
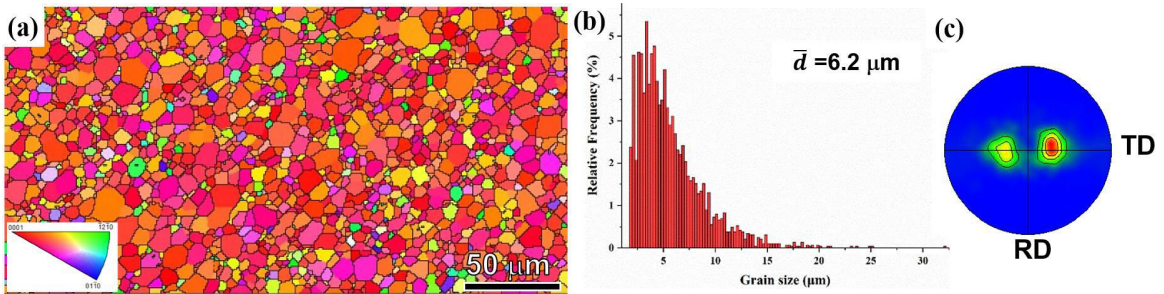

Figure 2. EBSD maps of as-received HP-Ti strip. (a) IPF map, (b) grain size distribution, (c) {0002} PF.
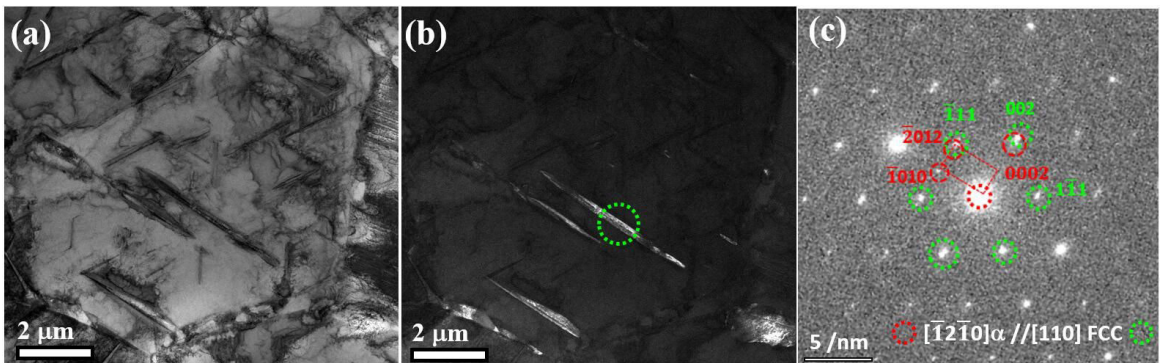

Figure 3. TEM images of as-received HP-Ti strip. (a) Bright field image, (b) Dark field image, (c) SAED pattern of the band marked by a dotted circle in (b).
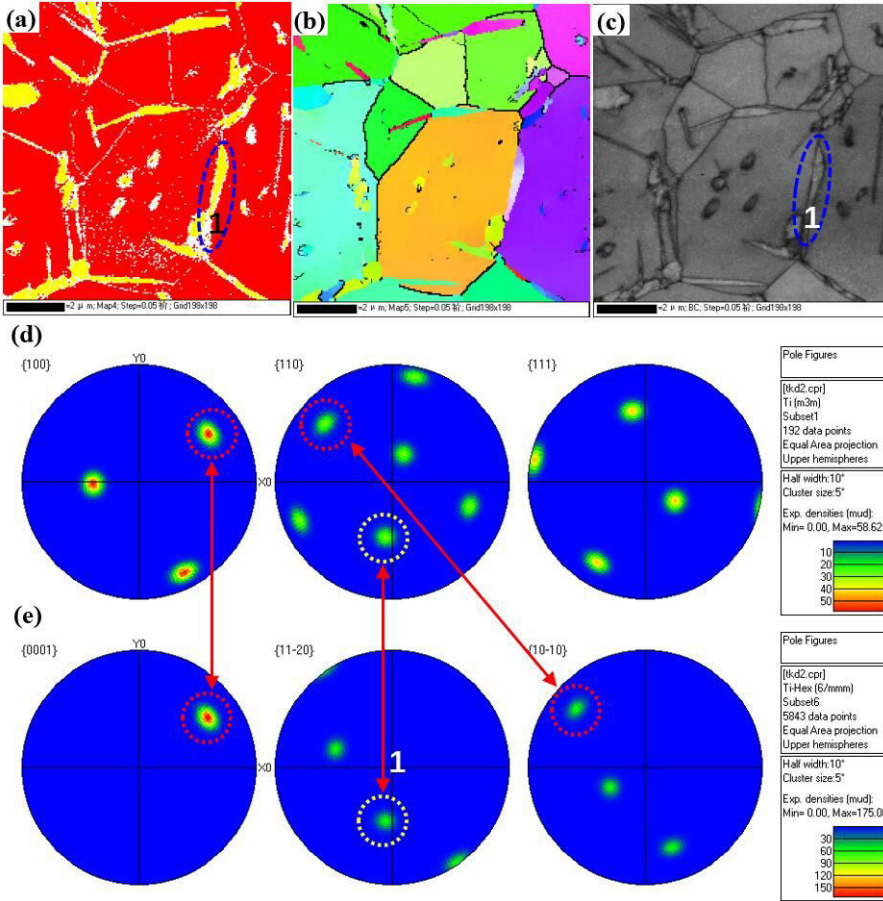
Figure 4. TKD analysis of the annealed strip: (a) two phases distribution, (b) IPF map; (c) Kikuchi band contrast map; (d) PFs of FCC-Ti phase; (e) PFs of HCP-Ti phase.
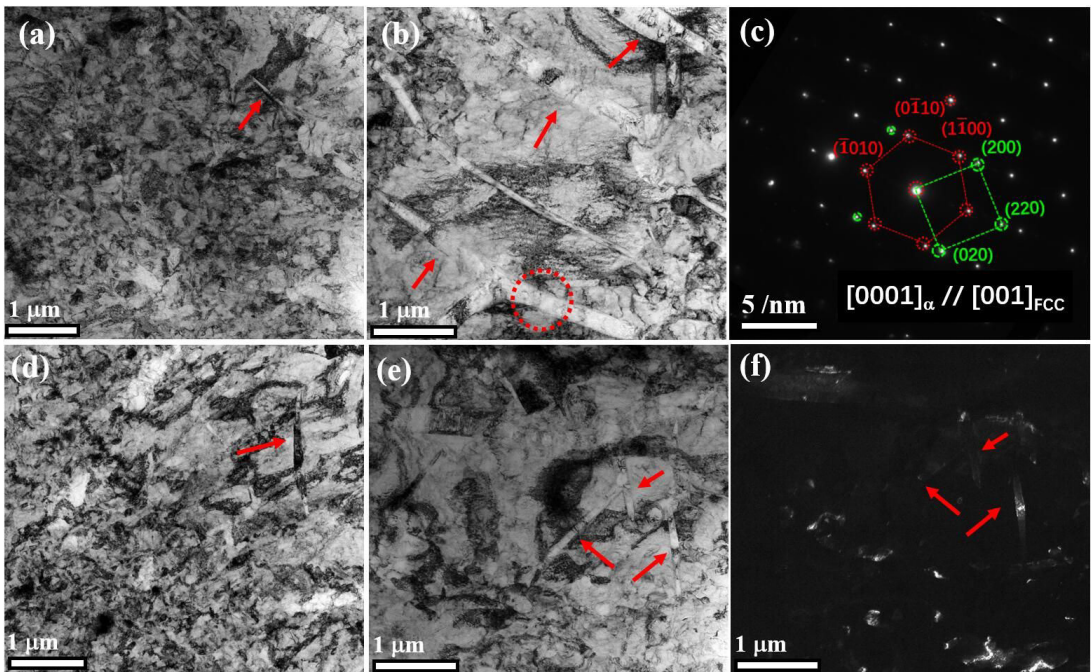

Figure 5. TEM images of 280 μm and 95 μm ultra-thin strips. (a−c) 280 μm, (d−f) 95 μm; (c) SAED pattern of the lath marked by a dotted circle in (b); (e, f) BF image and DF image, red arrows illustrate FCC phase.
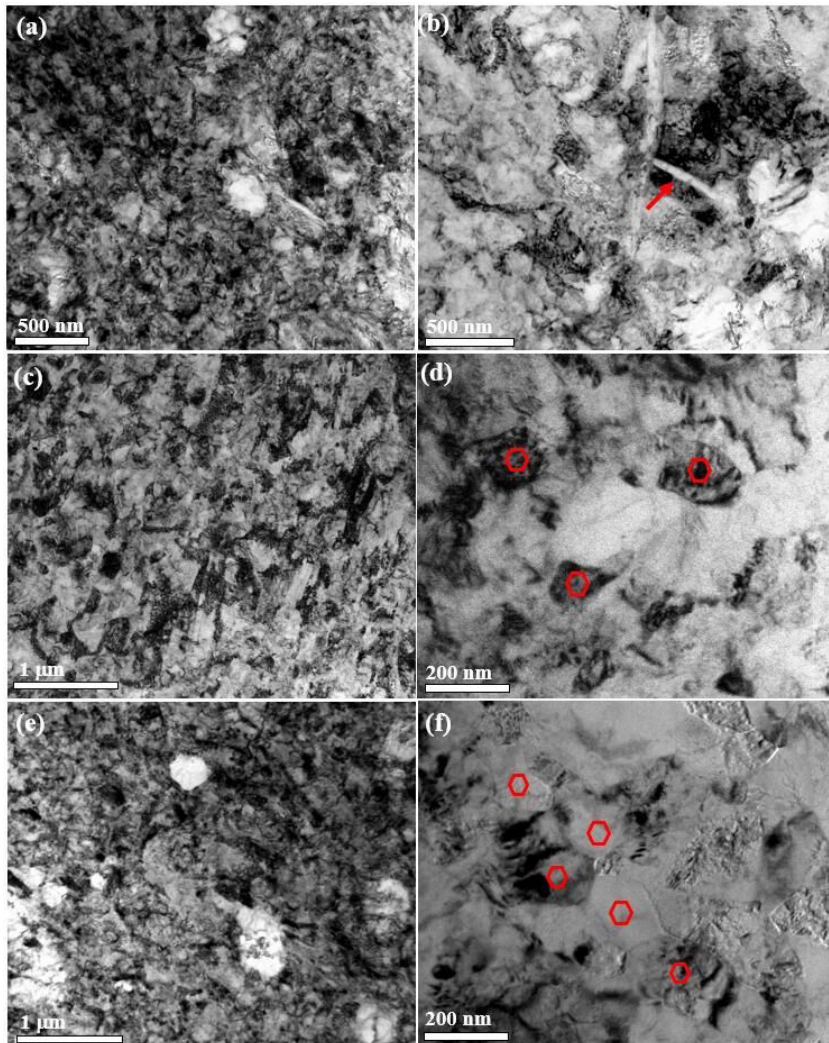
Figure 6. TEM morphology of ultra-thin strips. (a−b) 65 μm; (c−d) 30 μm; (e−f) 20 μm; red arrows illustrate FCC phase and hexagons mark the grains with clear boundaries.

Figure 6c–f show TEM images of ultra-thin strips that are 30 μm and 20 μm in thickness, and Figures 6(c,e) demonstrates the formation of a more homogenous ultra-fine grained microstructure. Subgrains/grains with distinct boundaries and a mean size of 360 nm were also found, as indicated by hexagons in Figure 6d. The ultra-fine grained microstructure of a 20 μm ultra-thin strip in Figure 6e has numerous large grains embedded within it. Figure 6f shows the presence of high-angle grain boundary (HAGB) subgrains/grains with an average size of 400 nm and a low dislocation density. Twin-free microstructures are created during rolling, which shows that dislocation slip is the main deformation mechanism. Dislocation arrangement causes LAGB to occur in slip-dominated grains due to the increased dislocation density. More dislocations are stored at LAGB and eventually converted to HAGB as a result of further deformation[27]. Grain boundaries become straight and the number of subgrains/grains increases as the dislocation density decreases[11]. This indicates that a higher deformation strain leads to dynamic recovery/recrystallization. With an increase in strain during the ECAP process or cold-rolling of CP-Ti, continuous dynamic recrystallization and LAGB changing into HAGB are observed as well[17,28,29].

Figure 7 illustrates the EBSD analysis of an ultra-thin strip with the width of 20 μm. Under the severe rolling strain, many small equiaxed grains are formed due to dynamic recovery/recrystallization in Figure 7a. The microstructure produced by the severe rolling consists of a combination of recrystallized grains, sub-grains, and deformed structures, as illustrated in Figure 7b. Substructure is dominant, accounting for 76% of the proportion, as seen in Figure 7c. This indicates that the HP-Ti ultra-thin strip is characterized by structural heterogeneity and high dislocation density, which is in line with the results of TEM in Figure 6. At the same time, the FCC lath structures almost disappear in 20 μm ultra-thin strips, according to EBSD analysis. Spheroidization of the lath structure and reversal of the FCC phase to the HCP phase are responsible for the disappearance of FCC phase[12]. In an FCC-Zr phase of the zircaloy-4 alloy, Guo et al.[26] have observed the reverse phase transformation from FCC to HCP.
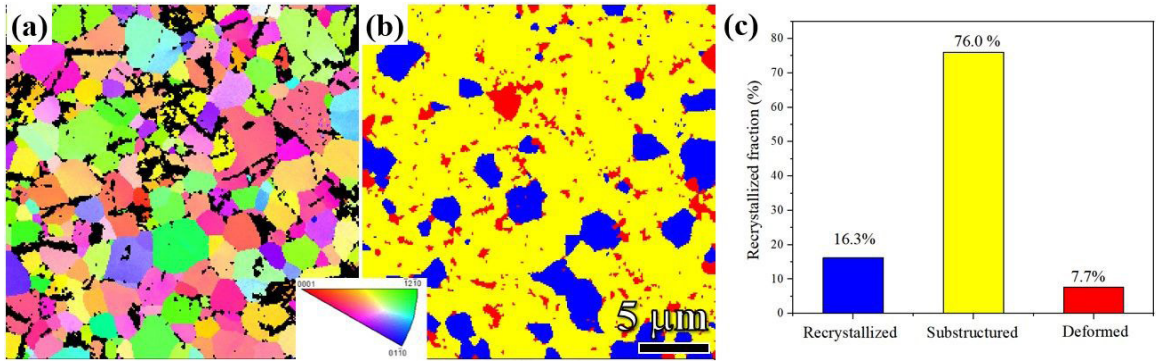
Figure 7. EBSD analysis of an ultra-thin strip with the width of 20 μm. (a) IPF map; (b) recrystallized map; (c) recrystallized fraction.
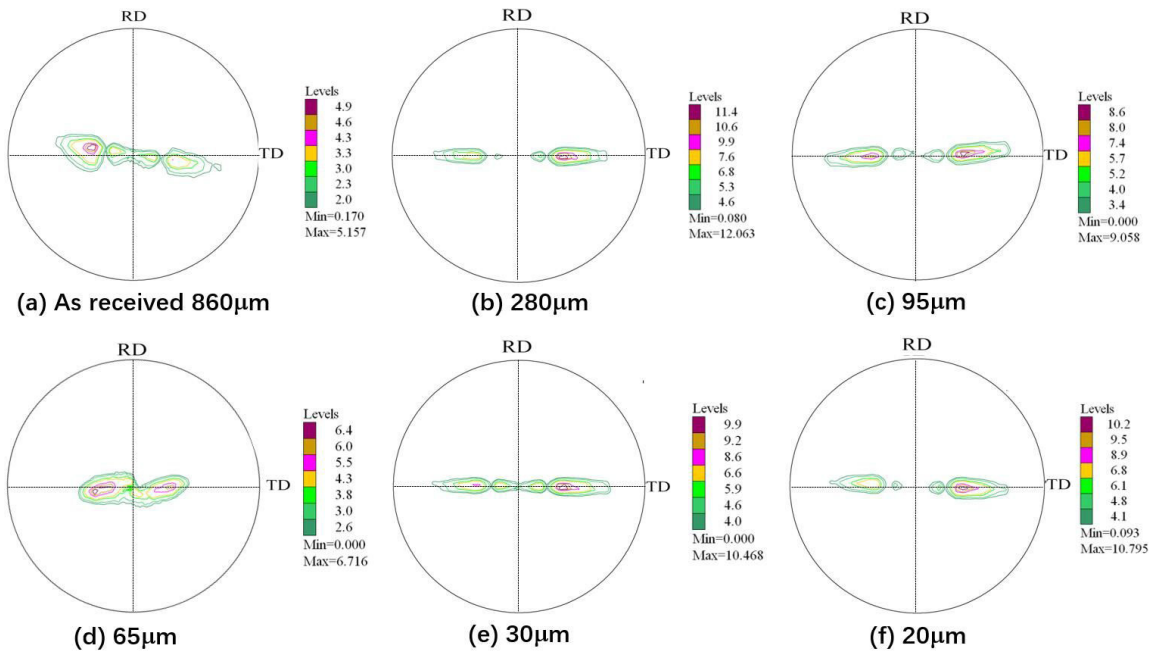

Figure 8. PFs of ultra-thin strips with different thicknesses.

3.3. Texture analysis

3.3.1. pole figures (PFs)

Figure 8 displays the PFs of the HP-Ti ultra-thin strips and the raw material. The PF of the raw material has a basal texture of the TD-split type consistent with the EBSD analysis in Figure 2c, which is a common texture in cold-rolled pure Ti[17,18]. Basal ND (the c-axis parallel to the normal direction of samples with a spread of 20°) and basal tilt (the c-axis tilted 40° from ND to TD) are the two components of the TD-split type basal texture, respectively[30]. In Figure 8a, basal ND and B basal tilt components have an orientation of ±17° and ±35 away from ND to TD, respectively. The TD-split type basal texture is also discovered to be 5° rotated clockwise along the ND axis. This indicates that the TD-split type basal texture is weak and scattered, with a maximum intensity of 5.2.

Figure 8 shows that the texture component in the ultra-thin strips remains unaltered except for 65 μm during the asymmetrical rolling operation. In the 280 μm thin strip, the basal ND texture component almost completely vanishes, whereas the basal tilt texture component is significantly improved and has a maximum intensity of 12.1. The maximum intensity lowers to 9.1 but the texture in the 95 μm ultra-thin strip is virtually the same as in the 280 μm ultra-thin strip. TD-split type basal texture in the 280 μm and 95 μm thin strips is symmetrically distributed on both sides of the RD axis, and rotates approximately 5° counterclockwise along the ND axis at the same time. TD-split type basal texture of the a 65 μm ultra-thin strip changes. On the one hand, the basal ND component vanishes. Comparable to the texture of raw materials, the basal tilt component, on the other hand, has a characteristic tilt of 32° from the ND to the TD and rotates about 6° clockwise along the ND axis. A weak basal ND texture component reappears at 30 μm and 20 μm ultra-thin strips, and the basal tilt component is symmetrically distributed on both sides of the RD axis. The maximum

intensity of texture significantly increases compared to the 65 μm ultra-thin strip.

The main texture maximum intensity of the raw material and the ultra-thin strips are shown in Figure 9. The lowest intensity is found in the raw material. The texture maximum
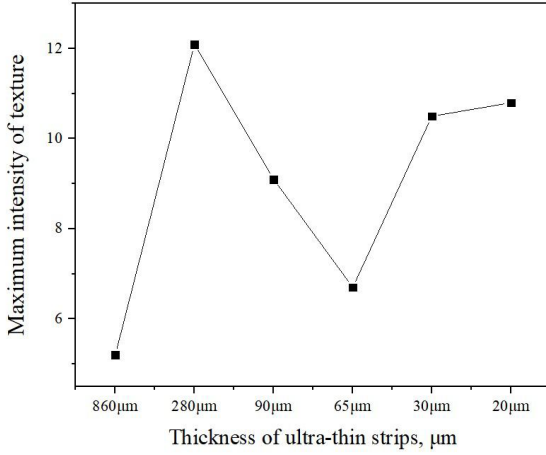

Figure 9. Maximum intensity of texture in the rolled ultra-thin strips with different thicknesses.

intensity changes significantly during the asymmetrical rolling process, with the 280 μm ultra-thin strip having the highest value. The maximum texture intensity decreases almost linearly from 280 μm to 65 μm ultra-thin strips, then increases once more as the thickness of the thin strip decreases further to 30 μm and 20μm. It denotes a dynamic spread of the grain orientation from the ND to the TD. Meanwhile, the material undergoes slight grain rotation along the ND axis during asymmetrical rolling.

3.3.2. Orientation distribution function (ODF) diagram

The major texture orientation of HCP CP-Ti is centered in the orientation distribution function (ODF) sections at 2 = 0° and 2 = 30°[31,32]. Figure 10 shows the ODF of the rolled samples in terms of the 0° and 30° sections. The Miller–Bravais indices of the rolling texture components for CP-Ti are listed in Table 1[20].

A weak component B ($\varphi_1 = 0°$, $\Phi = 40°$, $\varphi_2 = 0°$), which is characterized as tilted 40° from ND toward TD, dominates the texture of the as-received HP-Ti strip. In a 280 μm ultra-thin strip, there are two components: a strong component B and a weak component E. Component E is $\{0001\}\langle10\bar{1}0\rangle$ tilted 40° from ND toward TD. There
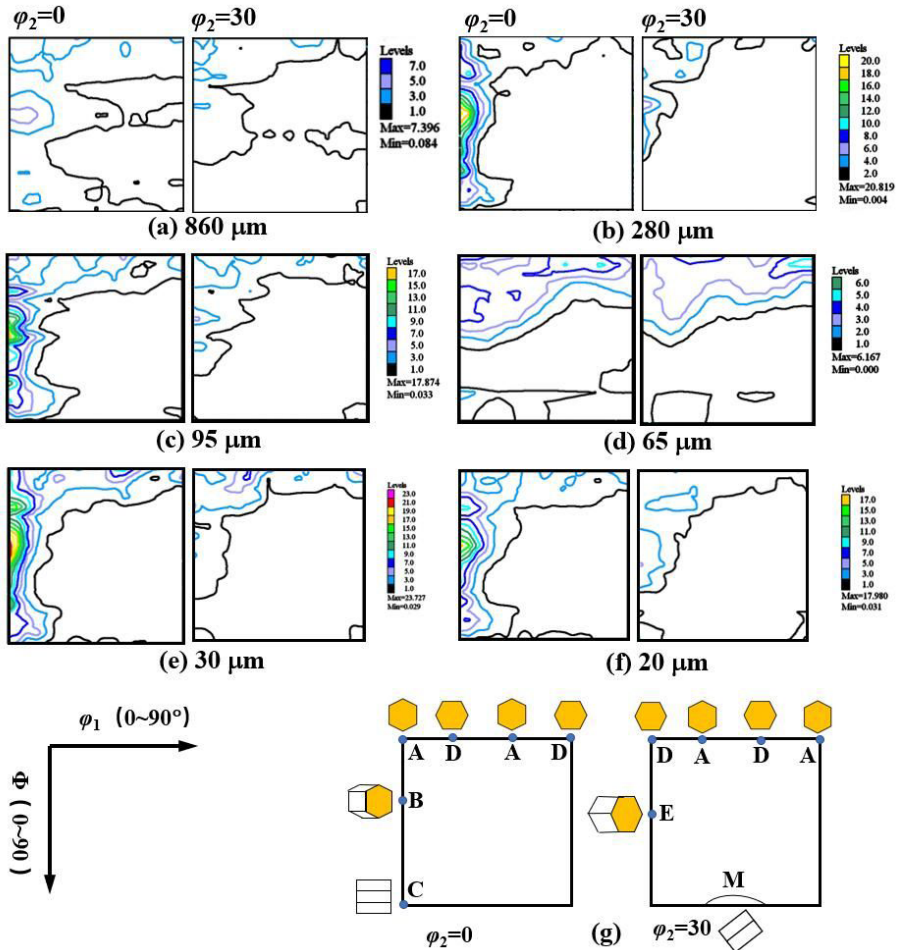

Figure 10. ODFs of HP-Ti ultra-thin strips with the thickness of (a–f) 860 μm−20 μm; (g) Schematic representation of texture components.

Table 1. Deformation Texture Components in Rolling of Titanium from Ref[20].

Texture Component	$(\varphi_1, \Phi, \varphi_2)$ (Bunge–Euler angles)	Description
E	0,40,30	$\{0001\}\langle11\bar{2}0\rangle$ tilted from ND toward TD
B	0,40,0	$\{0001\}\langle10\bar{1}0\rangle$ tilted from ND toward TD
M	50,90,30	$\{01\bar{1}0\}\langle2\bar{1}\bar{1}2\rangle$
D	30,0,0	$\{0001\}\langle11\bar{2}0\rangle$
A	0,0,0	$\{0001\}\langle10\bar{1}0\rangle$
C	0,90,0	$\{1\bar{1}22\}\langle10\bar{1}0\rangle$

Figure 11. Orientation intensities of ODFs in Figure 10.

is a strong component B with the strip reduced to 95 m, and weak components E ($\varphi_1 = 0°$, $\Phi = 40°$, $\varphi_2 = 30°$) and A($\varphi_1 = 0°$, $\Phi = 0°$, $\varphi_2 = 0°$) also emerged. Component A is characterized as $\{0001\}\langle11\bar{2}0\rangle$ tilted 40° from ND toward TD. When the thickness is reduced from 95 μm to 65 μm, texture intensity has substantially changed, component A has become stronger, component B has become weak and scattered, and component E has vanished. Comparatively to the 65 μm ultra-thin strip, component B in the 30 μm ultra-thin strip grew stronger and more aggregate, whereas component A maintained its intensity. A weak component E reappears at the same moment. There is a strong component B and a weak component E when the strips is reduced to 20 μm,and component A nearly disappeared.

A, B, and E are the three primary types of texture components found in all samples. Figure 11 displays the orientation intensity of these components for various ultra-thin strips. Three textural elements in the raw material had a low degree of intensity. The intensity of component B first increases in a 280 μm ultra-thin strip, then declines steadily to 65 μm, then rapidly increases when rolling to a 30 μm ultra-thin strip, finally decreases at 20 μm thick. Among all ultra-thin strips, except for 65 μm, component B has the highest intensity. The texture intensity of other components A and E is lower than that of component B, and changes gradually as the thickness of the strips gets thinner.

In HCP metals, texture evolution is significantly influenced by twinning and sliding[17,33]. The TEM study in Figures 3, 5, and 6 demonstrates that neither the raw material nor the ultra-thin strips of various thicknesses exhibit any twinning behavior. As a result, dislocation slipping is mostly responsible for the texture component evolution under rolling in Figure 11, according to Sahu et al.[34] have reported that the highest intensity components E and B are generated by a slip in CP-Ti under 90% rolling reduction. Zhong et al.[33] have found that all components E, B, and A can be ascribed to slip in cold-rolled CP Ti. Component B ($\varphi_1 = 0°$, $\Phi = 40°$, $\varphi_2 = 0°$) is typical of a dislocation basal slip tilted 40° from ND to TD. This indicates that, in ultra-thin strips other than 65 μm thickness in Figure 11, the dislocation basal slip of
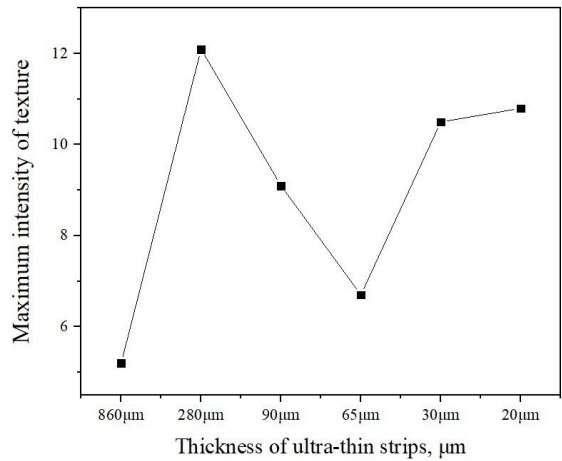
$\{0001\}\langle10\bar{1}0\rangle$ tilted 40° from ND toward TD is the primary factor driving the evolution of component intensity.

The intensity of component B in the 65 μm ultra-thin strip is the lowest compared to other ultra-thin strips and is about equal to the intensity of the other two components, A and E. This shows that other mechanisms are responsible for the intensity decreasing of component B during the rolling reduction to 65 μm. In Figure 8, the TD-split type basal texture is symmetrically distributed on both sides of the RD axis with an angle of ±38–40° from ND to TD in all ultra-thin strips other than that of 65 μm. However, in a 65 μm ultra-thin strip, the basal ND component vanishes, and the basal tilt component has the feature of angling 32° from the ND to the TD and rotating around 6° counterclockwise along the ND axis. Meanwhile, the maximum intensity of the basal tilt component is rapidly decreasing. This suggests that during the asymmetrical rolling, grain rotation takes place. When raw material with an 860 μm thickness is rolled into a 65 μm ultra-thin strip, severe plastic deformation causes grain rotation and grain boundary slip, which significantly reduces the maximum intensity of the texture component. As the thickness of the ultra-thin strip decreases to 30 μm at 96.5% strain and 20 μm at 97.8% strain, texture component B becomes the final stable component. With increase in asymmetrical rolling reduction along ND, the crystallographic orientation <0002> shifts closer to the ND and becomes tilted towards the ±TD direction. This is a result of the combined effects of prismatic and basal slip, which in turn stabilize texture component B and maintain the stability of the TD-split type basal texture even under high strain conditions[27].

The spheroidization of FCC laths and the FCC-Ti to HCP-Ti reverse phase change, as depicted in Figures 5 and 6, may also assist in decreasing the intensity of component B in the 65 μm ultra-thin strip in addition to grain rotation. The majority of FCC-Ti laths have vanished with the thickness reduction to 65 μm, although several FCC-Ti laths are still present in the 280 μm and 95 μm ultra-thin strips. As a result, in a 65 μm ultra-thin strip, grain rotation and FCC-Ti to HCP-Ti reverse phase transformation had a greater impact on texture evolution than the basal slip.
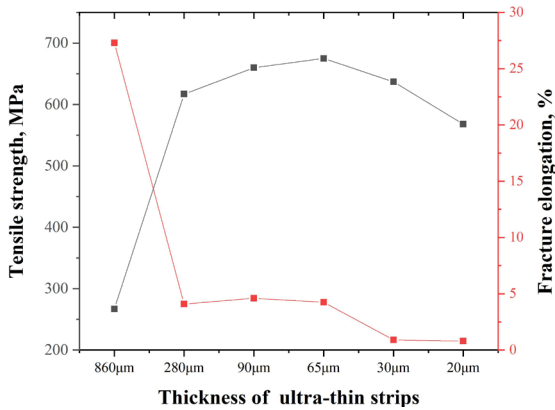
Figure 12. Dependence of tensile strength and fracture elongation on thickness of ultra-thin strips.

3.4. Mechanical property of ultra-thin strips

Figure 12 displays, as a function of ultra-thin strip thickness, the tensile properties and fracture elongation of the raw strip as well as the HP-Ti ultra-thin strip. The raw strip has a strength of 267 MPa and an elongation of 27.3%, respectively. The recrystallized raw strip a low strength and a high plasticity, which is compatible with the literature[19,28]. The tensile strength of the ultra-thin strip increases with decreasing thickness, peaking at 675 MPa at 65 μm and steadily declining to 568 MPa at 20 μm. When the raw material is rolled to a thickness of 280 μm, the elongation rapidly decreases, and then remains almost the same from 280 μm to 65 μm. Next, the elongation monotonically decreases with the rolling reduction to 20 μm. All ultra-thin strips have substantially lower elongations than the recrystallized raw material.

As can be seen in Figures 5 and 6, as the thickness is decreased, asymmetrical rolling results in a significant microstructural refinement and simultaneously increases the dislocation density. Consequently, with the rolling reduction, tensile strength increases while plasticity falls. When the ultra-thin strip is less than 65 μm thickness, dynamic recovery/recrystallization occurs, which slows the loss of dislocation density and causes LAGB to change into HAGB. At the same time, when the thin strip thickness is less than 65 μm, a declining tendency in elongation is observed. This is also found in the annealed ultra-thin strips, which have thicknesses between 200 μm and 5 μm[14]. In Figures 6c–f and 7, the strip consists of a mixture of recrystallized grains, sub-grains, and deformed structures. This structural heterogeneity leads to a reduction in fracture elongation.

4. Conclusions

1. When raw materials having a few FCC-Ti lath structures are rolled into ultra-thin strips with thicknesses ranging from 280 μm to 65 μm, equiaxed grains change into deformation structures with high dislocation density. Further rolling reduction results in the formation of an ultra-fine grained microstructure and the gradual disappearance of FCC-Ti laths.

When the thickness of ultra-thin strips is less than 65 μm, dynamic recovery/recrystallization occurs.

2. The basal texture of the TD-split type is evident in both the raw and HP-Ti ultra-thin strips; the texture intensity is lowest in the 65 μm ultra-thin strip.

3. All samples primarily consist of the texture components A, B, and E. Component B has the highest strength of the three in all ultra-thin strips except those that have a thickness of 65 μm; in 65 μm thick strips, the strength of components A, B, and E is very low.

4. Dislocation basal slip, tilted 40° from ND toward TD, is responsible for the high intensity of component B and its rolling-related texture evolution. Grain rotation and spheroidization of FCC laths, as well as FCC-Ti to HCP-Ti reverse phase transformation, diminish the intensity of component B in 65 μm thick ultra-thin strips.

5. The tensile strength of the ultra-thin strips increases with decreasing thickness, reaching a peak of 675 MPa at 65 μm and then gradually falling to 568 MPa at 20 μm. All ultra-thin strips show lesser elongation and higher strength compared to the raw strip because of the high dislocation density.

5. Acknowledgments

6. References

1. Mamilla VR, Chakradhar KS. Micro Machining for Micro Electro Mechanical Systems (MEMS). Procedia Materials Science. 2014;6:1170-7. http://doi.org/10.1016/j.mspro.2014.07.190.

2. Xiang HL, Meng S, Xiangkun S, QiLin Z, QingBo Y. Advances in research and application of foil rolling. Jixie Gongcheng Xuebao. 2017;53(10):1. http://doi.org/10.3901/JME.2017.10.001.

3. Liu X, Xiao H. Theoretical and experimental study on the producible rolling thickness in ultra-thin strip rolling. J Mater Process Technol. 2020;278:116537. http://doi.org/10.1016/j.jmatprotec.2019.116537.

4. Shou DC, Xiang HL, Li ZL, Song M. Crystal plasticity finite element simulation of slip and deformation in ultrathin copper strip rolling. Chin Shu Hsueh Pao. 2016;52(1):120-8. http://doi.org/10.11900/0412.1961.2015.00264.

5. Song M, Yin L, Bai F, Huang Z, Liu X. Size effect of ultra pure Ti thin strip under asymmetrical rolling. IOP Conf Series Mater Sci Eng. 2020;772:012087. http://doi.org/10.1088/1757-899X/772/1/012087.

6. Yu Q, Liu X, Sun Y. Formation of intermetallic compounds of Cu/Al multilayer foils during cold rolling. Sci China Mater. 2015;58(7):574. http://doi.org/10.1007/s40843-015-0070-1.

7. Qing BY, Xiang HL, Tang D. Extreme extensibility of copper foil under compound forming conditions. Sci Rep. 2013;3(1):3556. http://doi.org/10.1038/srep03556.

8. Bai F, Zhu Q, Shen J, Lu Z, Zhang L, Ali N, et al. Study on phase transformation orientation relationship of HCP-FCC

during rolling of high purity titanium. Crystals (Basel). 2021;11(10):1164.

9. Zherebtsov SV, Dyakonov GS, Salem AA, Sokolenko VI, Salishchev GA, Semiatin SL. Formation of nanostructures in commercial-purity titanium via cryorolling. Acta Mater. 2013;61(4):1167-78. http://doi.org/10.1016/j.actamat.2012.10.026.

10. Terada D, Inoue S, Tsuji N. Microstructure and mechanical properties of commercial purity titanium severely deformed by ARB process. J Mater Sci. 2007;42(5):1673-81. http://doi.org/10.1007/s10853-006-0909-7.

11. Wang GJ, Zhao XC, Yang XR, Liu XY. Texture evolution in commercially pure titanium after equal channel angular pressing at room temperature. Mater Sci Technol. 2013;29(8):961-7. http://doi.org/10.1179/1743284713Y.0000000234.

12. Bai F, Yin L, Zhao W, Zhou H, Song M, Liu Y, et al. Deformational behavior of face-centered cubic (FCC) phase in high-pure titanium. Mater Sci Eng A. 2021;800:140287. http://doi.org/10.1016/j.msea.2020.140287.

13. Hong DH, Lee TW, Lim SH, Kim WY, Hwang SK. Stress-induced hexagonal close-packed to face-centered cubic phase transformation in commercial-purity titanium under cryogenic plane-strain compression. Scr Mater. 2013;69(5):405-8. http://doi.org/10.1016/j.scriptamat.2013.05.038.

14. Wang S, Niu L, Chen C, Pang Y, Liao B, Zhong ZH, et al. Size effects on the tensile properties and deformation mechanism of commercial pure titanium foils. Mater Sci Eng A. 2018;730:244-61. http://doi.org/10.1016/j.msea.2018.06.009.

15. Jun QR, Qiao YS, Xiao L, Xiang DD, Sun J. Phase transformation behavior in titanium single-crystal nanopillars under 0001 orientation tension: A molecular dynamics simulation. Comput Mater Sci. 2014;92:8-12. http://doi.org/10.1016/j.commatsci.2014.05.018.

16. Klimova M, Zherebtsov S, Salishchev G, Semiatin SL. Influence of deformation on the Burgers orientation relationship between the α and β phases in Ti–5Al–5Mo–5V–1Cr–1Fe. Mater Sci Eng A. 2015;645:292-7. http://doi.org/10.1016/j.msea.2015.08.008.

17. Chun YB, Yu SH, Semiatin SL, Hwang SK. Effect of deformation twinning on microstructure and texture evolution during cold rolling of CP-titanium. Mater Sci Eng A. 2005;398(1):209-19. http://doi.org/10.1016/j.msea.2005.03.019.

18. Won JW, Park KT, Hong SG, Lee CS. Anisotropic yielding behavior of rolling textured high purity titanium. Mater Sci Eng A. 2015;637:215-21. http://doi.org/10.1016/j.msea.2015.03.096.

19. Milner JL, Abu-Farha F, Kurfess T, Hammond VH. Effects of induced shear deformation on microstructure and texture evolution in CP-Ti rolled sheets. Mater Sci Eng A. 2014;619:12-25. http://doi.org/10.1016/j.msea.2014.09.004.

20. Gurao NP, Sethuraman S, Suwas S. Evolution of texture and microstructure in commercially pure titanium with change in strain path during rolling. Metall Mater Trans, A Phys Metall Mater Sci. 2013;(44):1497-507. http://doi.org/10.1007/s11661-012-1484-y.

21. Kou WJ, Sun QY, Xiao L, Sun J. Plastic deformation-induced HCP-to-FCC phase transformation in submicron-scale pure titanium pillars. J Mater Sci. 2020;55(5):2193-201. http://doi.org/10.1007/s10853-019-04043-0.

22. Yang JX, Zhao HL, Gong HR, Song M, Ren QQ. Proposed mechanism of HCP→FCC phase transition in titianium through first principles calculation and experiments. Sci Rep. 2018;8(1):1992. http://doi.org/10.1038/s41598-018-20257-9.

23. Jing R, Liu CY, Ma MZ, Liu RP. Microstructural evolution and formation mechanism of FCC titanium during heat treatment processing. J Alloys Compd. 2013;552:202-7. http://doi.org/10.1016/j.jallcom.2012.10.083.

24. Yang M, Hu J, Cao S, Feng G, Yang Y, Liu R, et al. Influence of nonmetallic interstitials on the phase transformation between FCC and HCP titanium: a density functional theory study. Metals (Basel). 2022;12(10):1607. http://doi.org/10.3390/met12101607.

25. Guo W, Zhang Y, Ren J, Ali M, Wang Q, Yuan F, et al. Atomic scale understanding of the mutual transformations of 2H, 4H, 12R and 3C structures in face-centered cubic zirconium. J Nucl Mater. 2023;573:154138.. http://doi.org/10.1016/j.jnucmat.2022.154138.

26. Guo W, Han F, Li G, Zhang Y, Ali M, Ren J, et al. Atomic scale investigation of FCC → HCP reverse phase transformation in face-centered cubic zirconium. J Mater Sci Technol. 2023;137:8-13. http://doi.org/10.1016/j.jmst.2022.07.032.

27. Ghosh A, Singh A, Gurao NP. Effect of rolling mode and annealing temperature on microstructure and texture of commercially pure-titanium. Mater Charact. 2017;125:83-93. http://doi.org/10.1016/j.matchar.2017.01.022.

28. Gunderov DV, Polyakov AV, Semenova IP, Raab GI, Churakova AA, Gimaltdinova EI, et al. Evolution of microstructure, macrotexture and mechanical properties of commercially pure Ti during ECAP-conform processing and drawing. Mater Sci Eng A. 2013;562:128-36. http://doi.org/10.1016/j.msea.2012.11.007.

29. Zhao P, Chen B, Kelleher J, Yuan G, Guan B, Zhang X, et al. High-cycle-fatigue induced continuous grain growth in ultrafine-grained titanium. Acta Mater. 2019;174:29-42. http://doi.org/10.1016/j.actamat.2019.05.038.

30. Wang Y, He W, Liu N, Chapuis A, Luan B, Liu Q. Effect of pre-annealing deformation on the recrystallized texture and grain boundary misorientation in commercial pure titanium. Mater Charact. 2018;136:1-11. http://doi.org/10.1016/j.matchar.2017.11.059.

31. Bishoyi BD, Sabat RK, Sahu J, Sahoo SK. Effect of temperature on microstructure and texture evolution during uniaxial tension of commercially pure titanium. Mater Sci Eng A. 2017;703:399-412. http://doi.org/10.1016/j.msea.2017.07.081.

32. Wang YN, Huang JC. Texture analysis in hexagonal materials. Mater Chem Phys. 2003;81(1):11-26. http://doi.org/10.1016/S0254-0584(03)00168-8.

33. Zhong Y, Yin F, Nagai K. Role of deformation twin on texture evolution in cold-rolled commercial-purity Ti. J Mater Res. 2008;23(11):2954-66. http://doi.org/10.1557/JMR.2008.0354.

34. Sahu VK, Gupta S, Gurao NP. Effect of initial texture on the evolution of microstructure and texture during rolling of commercially pure titanium at room and cryogenic temperature. Metall Mater Trans, A Phys Metall Mater Sci. 2020;51(11):5848-60. http://doi.org/10.1007/s11661-020-05979-8.